



Correlation between magnetic properties and cationic distribution of $\text{Zn}_{0.85-x}\text{Ni}_x\text{Mg}_{0.05}\text{Cu}_{0.1}\text{Fe}_2\text{O}_4$ nano spinel ferrite: effect of Ni doping

S. N. Kane^{1,*} and M. Satalkar¹

¹Magnetic Materials Laboratory, School of Physics, D. A. University, Khandwa Road Campus, Indore 452001, India

Received: 24 June 2016

Accepted: 23 November 2016

Published online:
30 November 2016

© Springer Science+Business
Media New York 2016

ABSTRACT

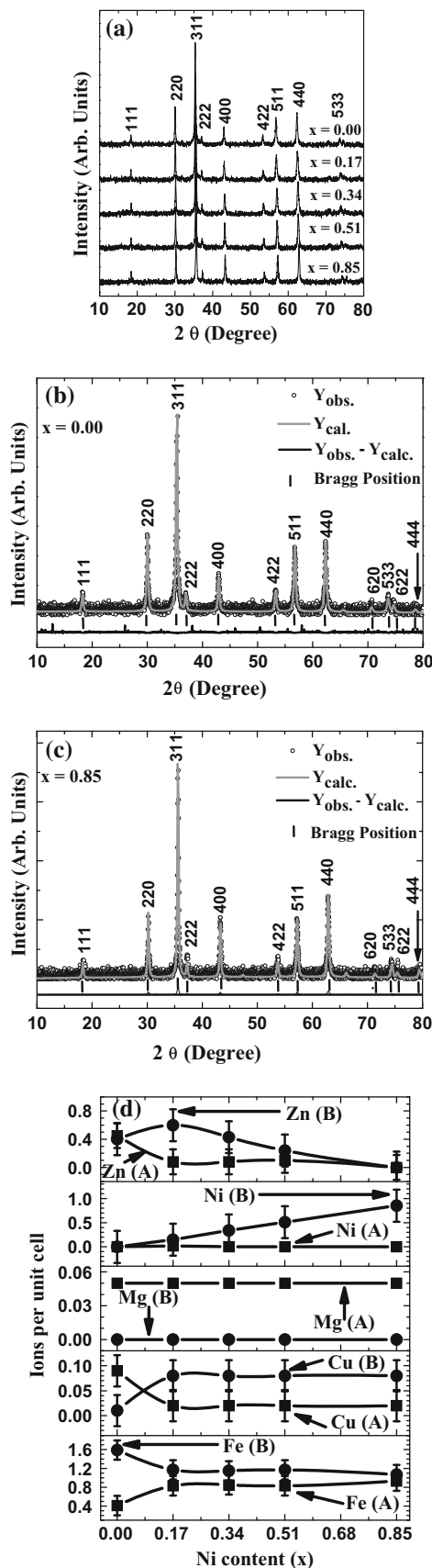
The correlation among magnetic properties and cationic distribution of Ni-doped $\text{Zn}_{0.85-x}\text{Ni}_x\text{Mg}_{0.05}\text{Cu}_{0.1}\text{Fe}_2\text{O}_4$ ($x = 0.00, 0.17, 0.34, 0.51, 0.85$) ferrite, synthesized using sol-gel auto-combustion process is studied by X-ray diffraction (XRD), scanning electron microscope (SEM), energy-dispersive X-ray analysis (EDAX), and magnetic measurements. XRD patterns revealed a pure phase spinel ferrite structure for all samples with Scherrer's grain diameter (D) ranging from 33.55 to 42.07 nm. Experimental, theoretical lattice constant ($a_{\text{exp}}, a_{\text{th}}$), specific surface area (S), and the distances between cations (M_e-M_e) (b, c, d, e, f) of the annealed Zn–Ni–Mg–Cu ferrite decrease with the increase in Ni doping. Elemental analysis, particle diameter, and surface morphology were examined by EDAX and SEM. Coercivity (H_c) and saturation magnetization (M_s) of Zn–Ni–Mg–Cu ferrite ranges between 0.97–167.5 Oe and 47.63–136.93 $\text{Am}^2 \text{kg}^{-1}$, respectively, signifying the soft character of annealed samples. Magnetic parameters such as H_c , magnetocrystalline anisotropy (K_1), remanence (M_r), and reduced remanent magnetization (M_r/M_s) increase up to $x = 0.51$ and then reduce thereafter with Ni doping. Particle size dependence of H_c reveals superparamagnetic, single domain, and multi-domain nature of the studied ferrite. Observed similar trend of M_s , Néel/experimental magnetic moment (n_B^N, n_B^e) with Ni content (x) follows the Néel's two-sublattice model of ferrimagnetism and is accredited to the cationic distribution and B–B exchange interaction. All these results establish a strong connection between magnetic properties and cationic distribution of $\text{Zn}_{0.85-x}\text{Ni}_x\text{Mg}_{0.05}\text{Cu}_{0.1}\text{Fe}_2\text{O}_4$ ferrite.

Address correspondence to E-mail: kane_sn@yahoo.com

Introduction

Technological growth in various scientific areas has engendered a potential need for the application of magnetic nanomaterials in several fields such as magnetic drug deliverance, hyperthermia, ferrofluids, storage devices, transformers, magnetic resonance imaging contrast, biomedical applications, and multilayer chip inductor (MLCI) [1–4]. In recent years, scientific and technological significance of spinel ferrite nanoparticles is increased due to their magnetic properties and wide range of applications especially when the particle size approaches to nanometer scale [5]. Spinel ferrites are known ferrimagnetic oxides with cations distributed at two different sublattices: tetrahedral (A) and octahedral [B] sites. Ideal spinel structure has cubic close-packed arrangement of anions, with 64 A and 32 B sites. A and B sites are fairly dissimilar from each other with reverence to their magnetic and structural environment and are sensitive to the chemical composition, preparation method, annealing temperature, and annealing time. Also the different types and amount of magnetic or non-magnetic cationic substitution on A and B sites strongly affect the exchange interactions among them. Thus, all these parameters turn out to be an important tool to tailor the structural and magnetic characteristics of ferrites. The magnetic properties of spinel ferrite originate from the spin magnetic moment of unpaired transition metal 3d electrons, coupled by the superexchange interaction via oxygen ions separating the magnetic ions. In ferrites, the exchange interaction occurs by the contribution of oxygen ‘anions’ which is called superexchange interaction. In ferrites, there are three probable superexchange interactions as follows: A–A, B–B, and A–B interaction. The inter-sublattice interactions (J_{AB} : A–O–B) are much stronger than the intra-sublattice interactions (J_{AA} : A–O–A and J_{BB} : B–O–B) in spinel ferrites with collinear ferrimagnetic structure. The inter-sublattice interaction (J_{AB} : A–O–B) is accountable for the discrepancy of initial permeability and Curie temperature of spinel ferrite [6, 7]. High initial permeability/saturation magnetization ($\mu_i \propto M_s^2$) is essential for dropping the number of layers of multilayer chip inductors (MLCI) to minimize the capacity between the layers and realizing miniaturization of the electronic components, with operating frequency up to 30 MHz [8].

The literature mainly focuses on the electromagnetic properties of Zn–Ni–Mg–Cu ferrite, but limited literature is available which reports magnetic properties and cationic distribution of Zn–Ni–Mg–Cu ferrite [7–11]. Sujatha et al. [8] investigated the structural and magnetic properties of Mg-substituted ann. (powder—500 °C/3 h, pellets—950 °C/1 h) $\text{Ni}_{0.5}\text{Cu}_{0.05}\text{Mg}_x\text{Zn}_{0.45-x}\text{Fe}_2\text{O}_4$ ($x = 0.09, 0.18, 0.27, 0.36, 0.45$). Results show a decrease in saturation magnetization and initial permeability and increase in coercivity, magnetocrystalline anisotropy constant, and Curie temperature with increasing Mg content. Sujatha et al. [9] examined the electromagnetic properties of Mg-substituted ann. (powder—500 °C/3 h, pellets—950 °C/1 h) $\text{Ni}_{0.5-x}\text{Mg}_x\text{Cu}_{0.05}\text{Zn}_{0.45}\text{Fe}_2\text{O}_4$ ($x = 0.1, 0.2, 0.3, 0.4$) ferrite. The results reveal a decrease in saturation magnetization, improved permeability, and reduced dielectric losses at higher frequencies with Mg substitution in Ni–Mg–Cu–Zn ferrite. Coercivity and anisotropy constant increases up to $x = 0.2$ and then reduces with increasing Mg content. Highest initial permeability was observed for the composition: $x = 0.1$. Sujatha et al. [10] also studied co-substitution effect of Mg and Zn on structural, magnetic, dielectric, and electrical properties of the ann. (powder—500 °C/3 h, pellets—950 °C/2 h) $\text{Ni}_{0.5-2x}\text{Mg}_x\text{Cu}_{0.05}\text{Zn}_{0.45+x}\text{Fe}_2\text{O}_4$ ($x = 0.0, 0.04, 0.08, 0.12, 0.16$) ferrite. Magnetization, coercivity, anisotropy constant, dielectric constant, and dielectric loss factor decrease with the substitution of Mg, Zn for Ni. The results depict improved permeability and enhanced sample resistance. Abdullah Dar et al. [11] studied the ann. (900 °C/5 h) $\text{Ni}_{0.5-x}\text{Cu}_{0.2}\text{Zn}_{0.3}\text{Mg}_x\text{Fe}_2\text{O}_4$ ($x = 0.0-0.4$) ferrite system and observed enhanced electrical resistivity and reduction of coercivity and dielectric losses with Mg content. Saturation magnetization increases up to $x = 0.2$ and decreases thereafter. Bachhava et al. [7] observed increase in the Curie temperature with nickel in $\text{Ni}_x\text{Mg}_{0.5-x}\text{Cu}_{0.1}\text{Zn}_{0.4}\text{Fe}_2\text{O}_4$ (ann. 1050 °C for 24 h) ($x = 0.1, 0.2, 0.3, 0.4, \text{ and } 0.5$) ferrite. Results show the increase in initial permeability with nickel content up to $x = 0.3$ and then decreases thereafter. The paper also reports a decrease in cationic distribution parameters such as bond lengths (R_A, R_B) and site radii (r_A, r_B) with nickel doping. Although the above-mentioned paper provides the parameters obtained by cationic distribution, it does not report the obtained cationic distribution. The cationic distribution can give an improved understanding of the



◀ **Figure 1** a X-ray diffraction patterns of $Zn_{0.85-x}Ni_xMg_{0.05}Cu_{0.1}Fe_2O_4$ (ann. 500 °C/3 h) system as a function of Ni content. Rietveld refinement for **b** $x = 0.00$ and **c** $x = 0.85$. **d** Cation distribution for tetrahedral (A) and octahedral (B) sites.

magnetic interaction in spinel ferrites. Thus, there exists a strong correlation between magnetic properties and cation distribution of spinel ferrite [12], which is still missing in the available literature [7–11]. Hence, it becomes important to have a broad knowledge of the cationic distribution in spinel ferrites.

Therefore, we report the correlation between magnetic properties and cation distribution of $Zn_{0.85-x}Ni_xMg_{0.05}Cu_{0.1}Fe_2O_4$ ferrite ($x = 0.00, 0.17, 0.34, 0.51, \text{ and } 0.85$) with Ni doping, prepared by sol-gel auto-combustion method.

Materials and methods

In this paper, a series of $Zn_{0.85-x}Ni_xMg_{0.05}Cu_{0.1}Fe_2O_4$ ($x = 0.00, 0.17, 0.34, 0.51 \text{ and } 0.85$) ferrites are synthesized by sol-gel auto-combustion method. For the synthesis of Zn–Ni–Mg–Cu spinel ferrite, stoichiometric amounts of citrate–nitrate/acetate precursors [Zinc nitrate— $Zn(NO_3)_2 \cdot 6H_2O$, Nickel acetate— $Ni(CH_3COO)_2 \cdot 4H_2O$, Magnesium acetate— $(CH_3COO)_2Mg \cdot 4H_2O$, Copper nitrate— $Cu(NO_3)_2 \cdot 3H_2O$, and Ferric nitrate— $Fe(NO_3)_3 \cdot 9H_2O$] were mixed with citric acid. The ratio between metal salt and fuel was taken 1:1. In the synthesis process, citric acid has a dual function: *initially, it acts as a chelator and then as fuel* [13]. The synthesis was carried out by dissolving all the precursors in stoichiometric ratio in deionized water, and then ammonia solution (NH_4OH) was added to maintain the pH at 7. Now the solution was heated at 120 °C in air till the loose powder (fluffy) was formed, called as ‘dry gel or as-burnt powder,’ which was then annealed at 500 °C for 3 h.

Structural studies were carried out by X-ray diffraction (XRD) using Bruker D8 advance diffractometer. XRD patterns were obtained using $Cu-K_{\alpha}$ radiation ($\lambda = 0.1540562 \text{ nm}$) at room temperature in θ – 2θ configuration using Bruker LynxEye detector (Silicon strip technology). Elemental analysis, particle size, and surface morphology of Zn–Ni–Mg–Cu ferrite samples were examined by energy-dispersive X-ray analysis (EDAX, INCA-OXFORD) and scanning electron microscope (SEM, JEOL-JSM5600). Room-temperature magnetic measurements of all the

compositions were performed using superconducting quantum interference device (SQUID) magnetometer (Quantum design MPMS) by applying maximum field: $H_{\max} = \pm 5$ T.

Data analysis

Cationic distribution of all the studied samples was estimated using X-ray diffraction intensities, employing Bertaut method [14]. The calculated and observed intensity ratios were matched for several combinations of cations distribution at (A) and [B] sites as described in [15]. The best cationic distribution among A and B sites for which theoretical and experimental ratios agree clearly is taken to be the correct one to calculate the cationic distribution parameters: ionic radii of A site (r_A) and B site (r_B), theoretical lattice constant (a_{th}), oxygen parameter ($u^{\bar{4}3m}$), interionic distances between cation and anion (M_e -O) (q, p), bond angles ($\theta_1, \theta_2, \theta_3, \theta_4$), tetrahedral/octahedral bond length (R_A, R_B), and the distances between cations (M_e - M_e) (b, c, d, e, f) as described in [16, 17]. The ionic radius involved in the above calculation has been taken from that reported by Shannon [18]. Experimental lattice constant (a_{exp}),

Figure 2 a, c, e, g, i Particle size distribution, SEM microstructures, (inset) and b, d, f, h, j EDS of $\text{Zn}_{0.85-x}\text{Ni}_x\text{Mg}_{0.05}\text{Cu}_{0.1}\text{Fe}_2\text{O}_4$ system, where a, b $x = 0.00$ c, d $x = 0.17$ e, f $x = 0.34$ g, h $x = 0.51$ i, j $x = 0.85$.

Scherrer's grain diameter (D), X-ray density (ρ_{XRD}), specific surface area (S), and magnetocrystalline anisotropy constant (K_1) were calculated as described in [19, 20]. Coercivity (H_C), remanence (M_r), reduced remanent magnetization or squareness ratio (M_r/M_s), and saturation magnetization (M_s) values were obtained by analyzing the hysteresis loops.

Results and discussions

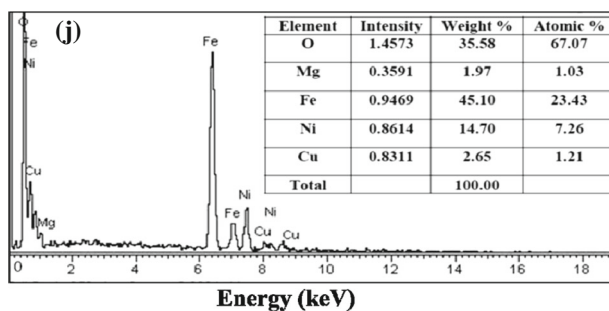
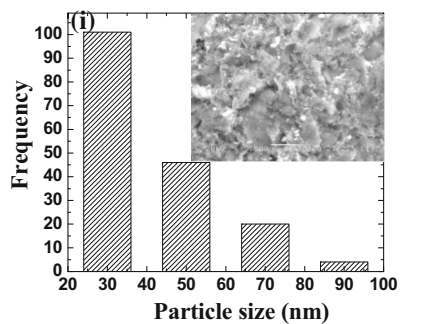
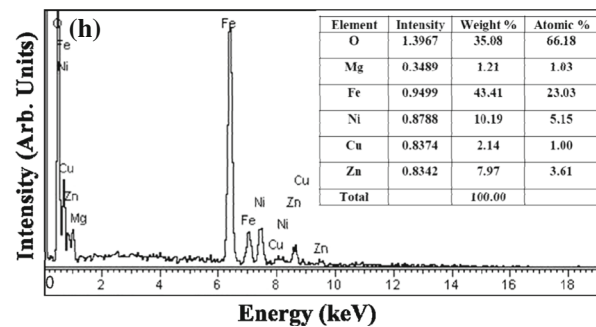
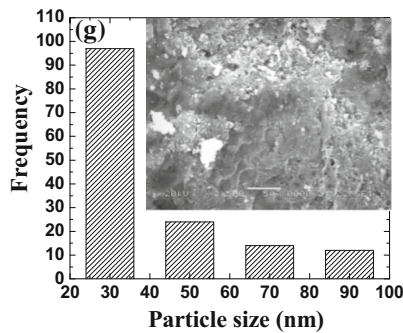
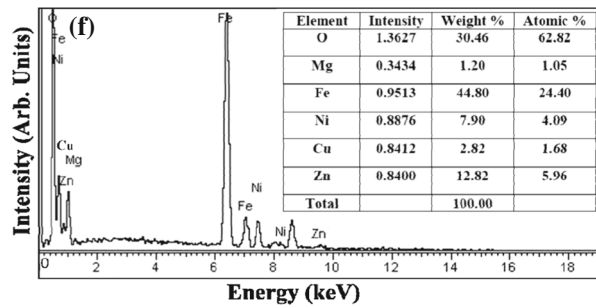
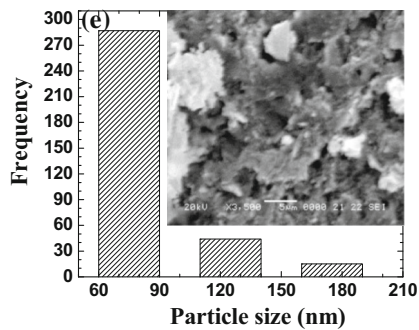
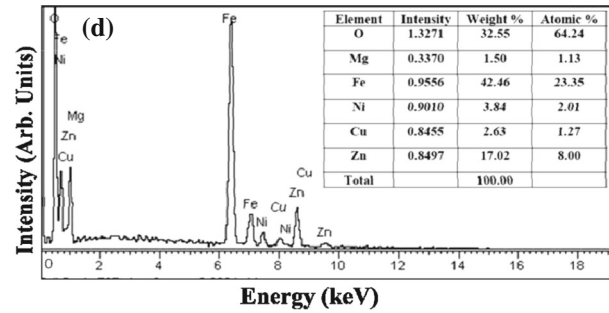
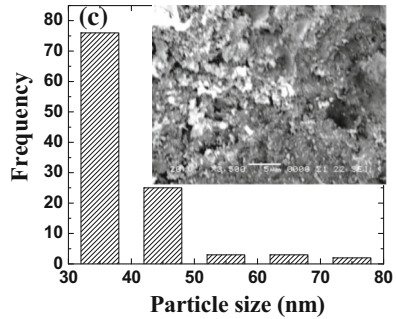
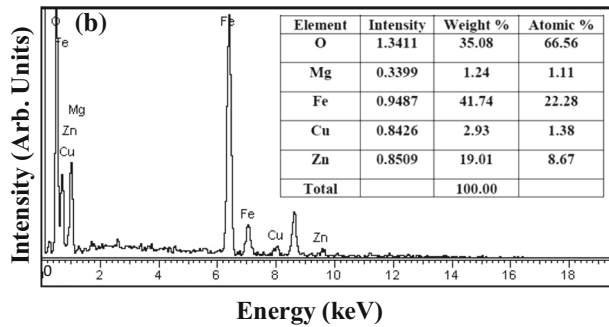
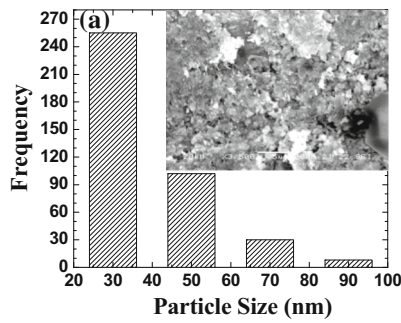
The indexed XRD patterns of $\text{Zn}_{0.85-x}\text{Ni}_x\text{Mg}_{0.05}\text{Cu}_{0.1}\text{Fe}_2\text{O}_4$ ($x = 0.00, 0.17, 0.34, 0.51, 0.85$) ferrite are presented in Fig. 1a. Rietveld refinement for $x = 0.00$ and $x = 0.85$, illustrated in Fig. 1b, c, respectively, was performed via material analysis using diffraction (MAUD) software [21]. Diffraction peaks confirm the formation of spinel phase similar to JCPDS card No. 08-0234 with (Fd3m) space group without showing any other detectable impurity peaks. The XRD patterns are sharper and broader than the as-burnt samples [22], indicating lower grain size of annealed samples.

Table 1 Experimental and theoretical lattice parameter ($a_{\text{exp}}, a_{\text{th}}$), ionic radii of A site (r_A) and B site (r_B), Scherrer's grain diameter (D), X-ray density (ρ_{XRD}) and specific surface area (S) of ann. 500 °C/3 h $\text{Zn}_{0.85-x}\text{Ni}_x\text{Mg}_{0.05}\text{Cu}_{0.1}\text{Fe}_2\text{O}_4$ system as a function of Ni content (x)

x	a_{exp} (nm) ± 0.0021	a_{th} (nm) ± 0.0025	r_A (nm) ± 0.0019	r_B (nm) ± 0.0006	D (nm) ± 3.71	ρ_{XRD} (Kg m^{-3}) ± 10.06	S ($\text{m}^2 \text{g}^{-1}$) ± 2.96
0.00	0.8412	0.8424	0.0551	0.0664	33.78	5329.46	33.33
0.17	0.8402	0.8397	0.0506	0.0680	33.55	5323.15	33.60
0.34	0.8377	0.8385	0.0504	0.0676	33.86	5345.37	33.15
0.51	0.8376	0.8375	0.0507	0.0671	40.39	5321.69	27.91
0.85	0.8352	0.8348	0.0496	0.0668	42.07	5316.06	26.83

Table 2 Ni content dependence of oxygen parameter ($u^{\bar{4}3m}$), tetrahedral/octahedral bond length (R_A, R_B) and the distances between cations (M_e - M_e) (b, c, d, e, f) of ann. 500 °C/3 h $\text{Zn}_{0.85-x}\text{Ni}_x\text{Mg}_{0.05}\text{Cu}_{0.1}\text{Fe}_2\text{O}_4$ system

x	u ± 0.0010	R_A (nm) ± 0.0019	R_B (nm) ± 0.0007	b (nm) ± 0.0007	c (nm) ± 0.0006	d (nm) ± 0.0009	e (nm) ± 0.0014	f (nm) ± 0.0013
0.00	0.3825	0.1931	0.2040	0.2974	0.3487	0.3643	0.5464	0.5151
0.17	0.3796	0.1886	0.2062	0.2971	0.3483	0.3638	0.5457	0.5145
0.34	0.3799	0.1884	0.2053	0.2962	0.3473	0.3627	0.5441	0.5130
0.51	0.3800	0.1887	0.2052	0.2961	0.3472	0.3627	0.5441	0.5129
0.85	0.3797	0.1876	0.2049	0.2953	0.3463	0.3617	0.5425	0.5115



The cationic distribution demonstrated in Fig. 1d for Zn–Ni–Mg–Cu nanoferrite is determined from the XRD intensities. Ni doping in Zn–Mg–Cu ferrite does not affect cationic distribution of Mg^{2+} ions at A and B sites. When Zn^{2+} ions are substituted by Ni^{2+} ions, the doped ions initially occupy both A and B sites, but for $0.17 < x \leq 0.85$, Ni^{2+} ions reside only at B site. Ni doping initially increases Zn^{2+} ions on B site and with further increasing Ni content, Zn^{2+} ion decreases on B site. Ni addition also decreases Cu^{2+} ions on A site and increases on B site. With the doping content, Fe^{3+} ions on B site decreases up to $x = 0.34$ and increases for $x = 0.51$ and then again decreases thereafter. It can be simply observed from Fig. 1d that except Mg^{2+} ions, all the cations are present at A and B sites leading to a mixed/disordered cationic distribution.

The cationic distribution achieved from the XRD intensities is in close conformity with the real distribution, as there is realistic agreement between theoretical ($a_{\text{th.}}$) and experimental ($a_{\text{exp.}}$) lattice parameters (Table 1). The observed decrease in ($a_{\text{th.}}$) and ($a_{\text{exp.}}$) can be understood by the fact that an element of higher ionic radius ($\text{Zn} = 0.060$ nm) is replaced by an ion with lower ionic radius ($\text{Ni} = 0.055$ nm). Ni content (x) dependence of A and B site ionic radii (r_A , r_B), Scherrer's grain diameter (D), X-ray density (ρ_{XRD}), and specific surface area (S) for ann. 500 °C/3 h $\text{Zn}_{0.85-x}\text{Ni}_x\text{Mg}_{0.05}\text{Cu}_{0.1}\text{Fe}_2\text{O}_4$ system is also depicted in Table 1. The variation in r_A and r_B can be credited to the migration of cations from one site to another. r_A decreases up to $x = 0.34$ and $x = 0.85$, due to enhancement and reduction of the population of smaller Fe^{3+} (0.049 nm) ions and larger Zn^{2+} (0.060 nm) ions, respectively, on A site. Increase in r_A for $x = 0.51$ can be accredited to decrease of Fe^{3+} ions and increase of Zn^{2+} ions on A site. Decrease in r_B with Ni content for ($0.17 < x \leq 0.85$) is due to decrease in concentration of larger Zn^{2+} ions (0.074 nm) and increase of smaller Ni^{2+} ions (0.069 nm) on B site. Increase in r_B for $x = 0.17$ can be ascribed to decrease in smaller Fe^{3+} ions (0.0645 nm) and increase in larger Ni^{2+} ions on B site. X-ray density (ρ_{XRD}) of annealed $\text{Zn}_{0.85-x}\text{Ni}_x\text{Mg}_{0.05}\text{Cu}_{0.1}\text{Fe}_2\text{O}_4$ ferrite system decreases for all values of x except for $x = 0.34$. Decrease in ρ_{XRD} can be accredited to decrease of unit cell mass which overtakes the reduction of unit cell volume. Increase in Scherrer's grain diameter (D) with increasing Ni content may be due to the grain boundary dispersion. Grain growth occurs due to grain boundary dispersion

as the activation energy for grain boundary dispersion is less than the lattice dispersal. Low activation energy of Ni for diffusion is one of the reasons for improved grain size. Specific surface area of particles (S) is the summation of the areas of the exposed surfaces of the particles per unit mass. Ferrites play an important role in improving the solid catalysts performance [23] due to their superior surface to bulk ratio. There is an inverse relationship between particle size and density with surface area. In general, high surface area implies small particle size. The smaller is the particle size, the larger is the surface area. Specific surface area of annealed particles decreases with increase in Ni content. After annealing, S decreases which is attributed to increase in particle size.

Table 2 represents the Ni content dependence of oxygen positional parameter (u^{43m}), tetrahedral/octahedral bond length (R_A , R_B), and the distances between cations (M_e-M_e) (b , c , d , e , f). Variation in R_A , R_B can be elucidated via u parameter. The oxygen parameter or anion parameter (u^{43m}) is a quantity which represents movement of O^{2-} ion due to substitution of cation at tetrahedral A site. As u increases, oxygen ions move in such a way that the distance between A and O ions (R_A) is increased, while that between B and O ions (R_B) is decreased and when u parameter decreases the O^{2-} ions are displaced in such a way that R_A decreases and R_B increases. It is of value to note that the calculated u parameter values are greater than the ideal value ($u_{\text{ideal}}^{43m} = 0.375$) for entire $\text{Zn}_{0.85-x}\text{Ni}_x\text{Mg}_{0.05}\text{Cu}_{0.1}\text{Fe}_2\text{O}_4$ nanoferrite. The highest value of u parameter is obtained for $x = 0$.

It implies that Ni addition reduces the distortion in spinel structure. Decrease in interionic distances between cations (b , c , d , e , f) is due to the replacement of Zn^{2+} by Ni^{2+} ion, as ionic radius of Zn^{2+} ion is greater than Ni^{2+} ion.

The microstructure of Ni-doped Zn–Mg–Cu spinel ferrites examined by the SEM technique given in inset of Fig. 2a, c, e, g, i clearly depicts the non-homogeneous particle size dispersal. The particle agglomeration with different shapes is distinctly visible in the SEM micrograph. Difference in sample microstructure indicates the presence of different metal ions: Zn, Ni, Mg, Cu, and Fe play a crucial role on the microstructure of prepared spinel ferrite. The distribution of particle size obtained through analyzing the SEM images via ImageJ software [24] is

described in Fig. 2a, c, e, g, i. The maximum size of the agglomerates mainly lies in the range of 24.11–35.86, 31.98–37.92, 59.92–89.84, 24.06–35.96 and 24.06–35.96 nm, respectively, for $x = 0.00, 0.17, 0.34, 0.51,$ and 0.85 . It is of value to note that the particle size distribution for $x = 0.00, 0.51,$ and 0.85 is almost alike and the maximum size of the agglomerates also lies in the similar range. Figure 2e, g corresponds to a broad distribution of particle size as compared with the other samples. The composition of Zn–Ni–Mg–Cu spinel ferrites has been determined using EDAX technique. EDAX spectra represented in Fig. 2b, d, f, h, j confirm the existence of all elements (Zn, Ni, Mg, Cu, Fe, O) in samples. The EDAX results distinctly indicate that all the precursors are very well reacted with each other to finally form the desired ferrite composition.

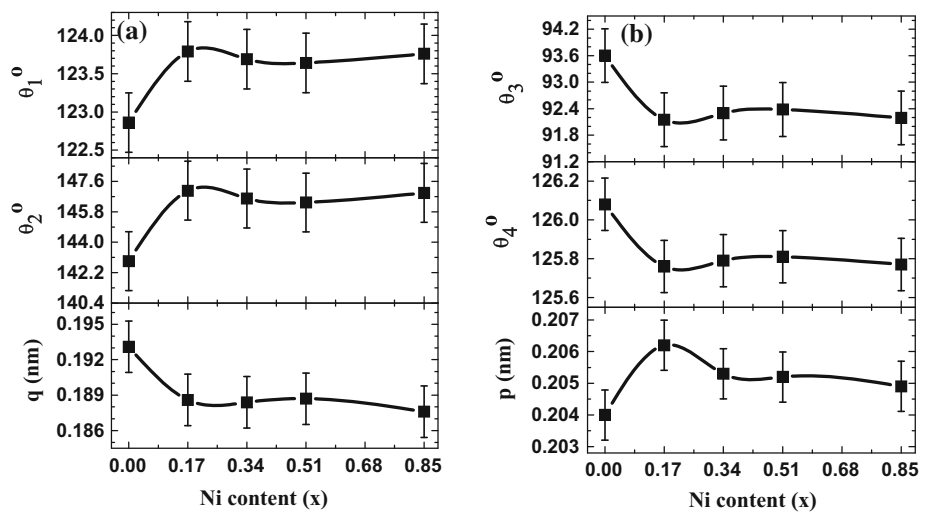
Ni content dependence of the bond angles $\theta_1, \theta_2, \theta_3, \theta_4,$ and distance between cation and anion (q, p) is illustrated in Fig. 3a, b. The bond angles $\theta_1, \theta_2,$ are the angles between A–O–B, whereas q is distance between the metal ions at A site and anion. Figure 3a shows the increase in bond angles θ_1, θ_2 and decrease in distance between the metal ions at A site and anion (q) for $x = 0.17$ and $0.85,$ indicating strengthening of A–B interaction. For $0.17 < x < 0.85,$ θ_1, θ_2 decreases and q increases suggesting weakening of A–B interaction. The bond angles θ_3, θ_4 decreases and the distance between the metal ions at octahedral site and anion (p) increases for $x = 0.17$ and 0.85 (Fig. 3b), indicating weakening of B–B interaction. For $0.17 < x < 0.85,$ θ_3, θ_4 increases and p decreases

suggesting strengthening of B–B interaction. The magnetic exchange (A–B, A–A and B–B) strength depends upon the bond distance and bond angles. The strength varies directly with bond angle and varies inversely with bond length.

Magnetization M ($\text{Am}^2 \text{kg}^{-1}$) versus the applied magnetic field H (Oe) at room temperature for the annealed $\text{Zn}_{0.85-x}\text{Ni}_x\text{Mg}_{0.05}\text{Cu}_{0.1}\text{Fe}_2\text{O}_4$ spinel nanoferrites for different compositions ($x = 0.00, 0.17, 0.34, 0.51, 0.85$) is illustrated in Fig. 4. Figure 4 inset represents the magnified area of the M – H curve in the region of the origin from that coercivity is determined. The saturation magnetization for $x = 0.0, 0.17,$ and 0.34 is obtained by plotting M versus $1/H$ curve and extrapolating data to $1/H = 0$ [25], as the samples are not saturated even at maximum magnetic field of 5 T.

Table 3 shows the remanence (M_r), reduced remanent magnetization/squareness ratio (M_r/M_s), coercivity (H_c), and magnetocrystalline anisotropy (K_1). M_r and M_r/M_s values determined from the M – H curve of the studied annealed Zn–Ni–Mg–Cu ferrite system, respectively, ranges between 0.27 – $19.71 \text{ Am}^2 \text{kg}^{-1}$ and 0.0 – 0.3 . According to the Stoner–Wohlfarth (SW) model, for an assembly of non-interacting 3D random particles, $M_r/M_s = 0.5$ (for randomly oriented uniaxial anisotropic ferromagnetic particles [26–28]). It is worth noting that SEM images (Fig. 2) reveal large particle agglomerates, composed of numerous grains and/or crystallites with dimension of the order of few tens of nm which are interacting among themselves. For studied samples, $M_r/$

Figure 3 a Variation of the bond angles ($\theta_1^{\text{A-O-B}}, \theta_2^{\text{A-O-B}}$) and distances between tetrahedral cation and anion ($M_c\text{-O}$) (q). b Variation of the bond angles ($\theta_3^{\text{B-O-B}}, \theta_4^{\text{B-O-B}}$) and distances between octahedral cation and anion ($M_c\text{-O}$) (p) for $\text{Zn}_{0.8-x}\text{Ni}_x\text{Mg}_{0.1}\text{Cu}_{0.1}\text{Fe}_2\text{O}_4$ system with Ni content (x).



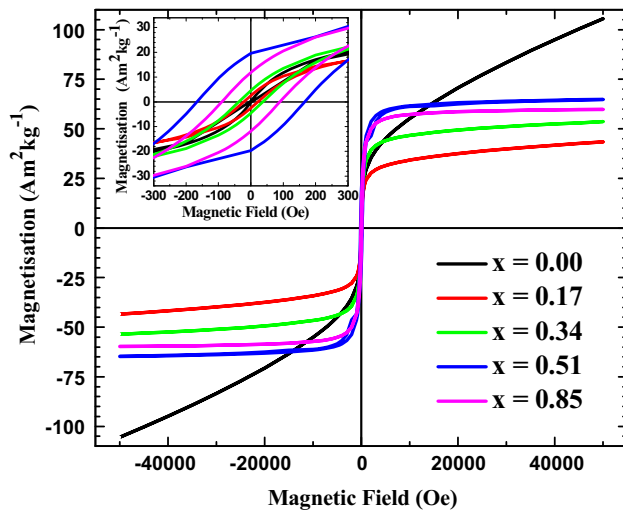


Figure 4 Room-temperature magnetization with applied magnetic field as a function of Ni content. *Inset* Magnified region of M–H curve to determine coercivity.

M_s values range between 0.0 and 0.3, which are lower than 0.5, ascribable to much stronger interactions among grains [28] and aggregates of particles are multi-domains. Therefore, SW model would be less relevant in our case and hence, it cannot be said evidently (using M_r/M_s values) that the sample possesses uniaxial anisotropy.

Coercivity is the magnetic field strength required to exceed the anisotropic barrier and allows the magnetization of the nano magnetic particles. The coercivity of polycrystalline material is associated to many factors such as grain size, porosity, nature of cation, and magnetocrystalline anisotropy. Coercivity (H_c) and magnetocrystalline anisotropy constant (K_1) of $\text{Zn}_{0.85-x}\text{Ni}_x\text{Mg}_{0.05}\text{Cu}_{0.1}\text{Fe}_2\text{O}_4$ increase up to $x = 0.51$ and then decrease thereafter. The variation in H_c is attributed to magnetocrystalline anisotropy. K_1 of NiFe_2O_4 is greater than that of ZnFe_2O_4 [16] and when Zn^{2+} ions are substituted by Ni^{2+} ions, K_1 increases and hence, coercivity also increases. But for

$x = 0.85$, K_1 decreases and thereby H_c also decreases. Decrease in K_1 can be described by the single ion anisotropy model [29]. According to this model, Fe^{3+} ions on A and B sites contribute to anisotropy energy. K_1 is then specified by relative combination of Fe^{3+} ions at A site (positive anisotropy) which is remunerated by Fe^{3+} ions at B site (negative anisotropy). With Ni doping, cationic re-distribution of Fe^{3+} ions modifies, which yields different concentrations of Fe^{3+} ions on A, B sites, and thus affects K_1 . It is apparent from Table 3 that the low values of squareness ratio (0.00–0.09), coercivity (0.97–37.14 Oe.), and non-saturated hysteresis loops confirm the superparamagnetic character of the ferrites with the compositions: $x = 0.00, 0.17, \text{ and } 0.34$.

Coercivity (H_c) also depends on the grain diameter (D). Perusal of Fig. 5a shows that coercivity increases with the grain diameter up to $x = 0.51$ and then decreases for $x = 0.85$. The grain size of the present system up to Ni content: 0.51 lies in the single domain region. In the single domain region, which arises when the grain size is smaller than a critical value, D_c (in our case critical value is 40.39 nm), the coercivity is expressed as [30]: $H_c = g - \frac{h}{D^{3/2}}$, where g and h are the constants and D is the particle diameter. The particle size which is in the range $0.51 < x \leq 0.85$ lies in the multi-domain region. The variation of coercivity with particle or crystallite size in the multi-domain configuration is expressed as [31]: $H_c = a + \frac{b}{D}$, where a and b are the constants. When the grain size is larger than the critical size (D_c), H_c is governed by the magnetic displacement; hence, the value of coercivity is small. When particle size is reduced to D_c , H_c then decided by magnetic domain rotation, so H_c reaches the maximum, and when particle size is less than D_c , H_c will be decreased for existence of superparamagnetism, for the region ($x = 0.0\text{--}0.34$).

Figure 5b displays the saturation magnetization (M_s), experimental magnetic moment (n_B^e), and Néel

Table 3 Remanence (M_r), squareness ratio (M_r/M_s), coercivity (H_c) and magnetocrystalline anisotropy constant (K_1) of ann. 500 °C/3 h $\text{Zn}_{0.85-x}\text{Ni}_x\text{Mg}_{0.05}\text{Cu}_{0.1}\text{Fe}_2\text{O}_4$ system as a function of Ni content (x)

x	$M_r \pm 7.11$ ($\text{Am}^2 \text{kg}^{-1}$)	$M_r/M_s \pm 0.10$	$H_c \pm 8.96$ (Oe)	$K_1 \pm 3.26$ ($\times 10^3 \text{ erg cm}^{-3}$)
0.00	0.27	0.00	0.97	0.7374
0.17	2.54	0.05	21.83	5.7653
0.34	4.60	0.08	37.14	11.8039
0.51	19.71	0.30	167.50	60.2511
0.85	11.87	0.20	90.09	29.8076

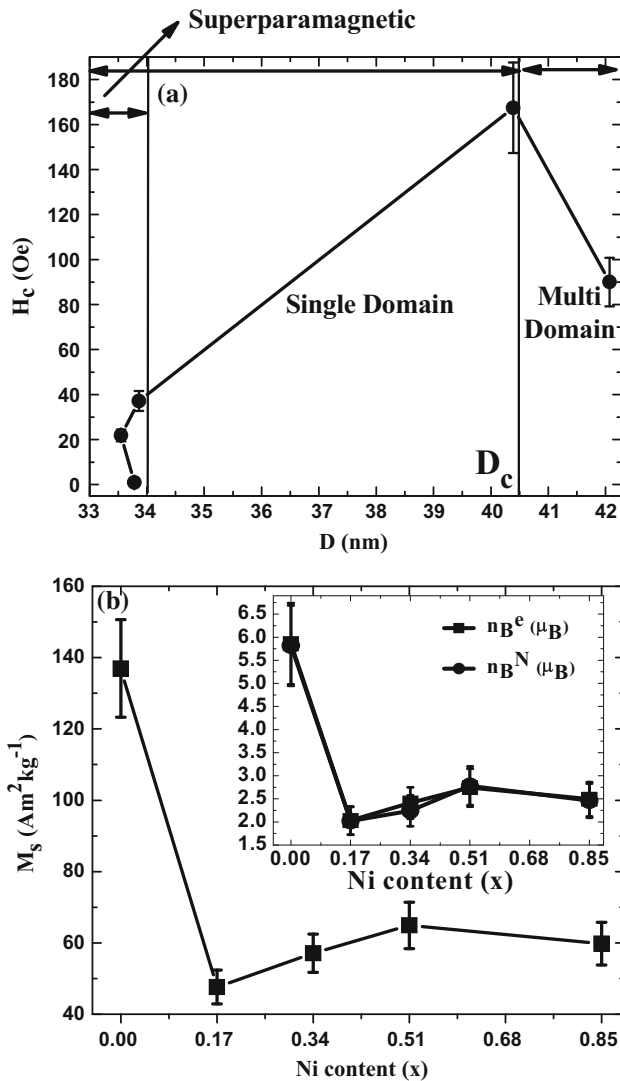


Figure 5 **a** Particle size dependence of coercivity (H_c) for $\text{Zn}_{0.85-x}\text{Ni}_x\text{Mg}_{0.05}\text{Cu}_{0.1}\text{Fe}_2\text{O}_4$ system. **b** Ni content dependence of saturation magnetization (M_s) and experimental and Néel magnetic moment (n_B^e , n_B^N) (Fig. 4b inset).

magnetic moment (n_B^N) with Ni content (Inset of Fig. 5b). Saturation magnetization (M_s) depends on grain size, initial permeability, cation distribution, and A–B exchange interactions [7, 32, 33]. M_s of the present system ranges between 47.63 and 136.93 $\text{Am}^2 \text{kg}^{-1}$. M_s , n_B^e , and n_B^N follow the similar trend with the doping content. Hence, the magnetization behavior of Zn–Ni–Mg–Cu ferrite can be enlightened according to Néel’s two-sublattice model of ferrimagnetism [16]. According to Néel’s model, the cationic magnetic moments on A and B sites are allied anti-parallel to each other forming a collinear structure with certain resultant magnetization

$M = M_B - M_A$, where M_A and M_B are, respectively, magnetic moment of A and B sites.

The observed saturation magnetization values initially decrease for $x = 0.17$, increase up to $x = 0.51$, and thereafter decrease again for $x = 0.85$. For $x = 0.0$ and 0.85 , Ni^{2+} ion forces Fe^{3+} ions to migrate from B to A site; thus, Fe^{3+} ions decreases and Ni^{2+} ions increases on B site which decreases magnetic moment at B site (M_B) and thus the net magnetic moment ($M_B - M_A$) decreases. Increase in M_s up to $x = 0.51$ is due to decrease of diamagnetic ion Zn^{2+} , and increase of Ni^{2+} ion on B site which in turn increases the B site magnetic moment and thus the magnetization increases. It is of value to note that the deviation of the bond angles θ_3 , θ_4 (Fig. 3b) and M_s with Ni content are quite similar. Hence, B–B exchange interaction is also responsible for the magnetization disparity with Ni content. A similar trend of M_s , n_B^e , n_B^N , θ_3 , and θ_4 with Ni content forms a strong association between magnetic properties and cationic distribution, which can be used effectively for tuning magnetic properties of ferrite.

Conclusions

Ni-doped Zn–Mg–Cu spinel ferrite was synthesized by sol–gel auto-combustion method. XRD confirms the single-phase spinel Zn–Ni–Mg–Cu ferrite structure with the grain size (D) of the nanoferrites in the range of 33.55–42.07 nm. Decrease of experimental, theoretical lattice parameter, (a_{exp} , a_{th}), and distances between cations (M_e – M_e) (b , c , d , e , f) with increasing Ni content can be attributed to relative larger ionic radii of Zn^{2+} as compared to Ni^{2+} ion. The observed variation in oxygen parameter (u^{43m}), tetrahedral/octahedral bond length (R_A , R_B), A and B site ionic radii (r_A , r_B) can be accredited to the migration of cations from A to B site or vice versa. Particle size distribution obtained from the SEM images for $x = 0.00$, 0.51 , and 0.85 observed to be identical and agglomerate size also lies in the comparable range. EDAX confirms the existence of all elements: Zn, Ni, Mg, Cu, Fe, and O in the spinel ferrite. The magnetic parameters such as coercivity (H_c), remanence (M_r), squareness ratio (M_r/M_s), and magnetocrystalline anisotropy constant (K_1) increase for all values of Ni concentration (x) except for $x = 0.85$. The variation in H_c is attributed to the magnetocrystalline anisotropy.

Particle size dependence of H_c was also studied. Observed variation in saturation magnetization (M_s) with Ni doping can be understood as a collective effect of cationic distribution and B–B exchange interaction.

Acknowledgements

This work is supported by MPCST Project No. 1783/CST/R & D/Phy and Engg Sc and by UGC-DAE CSR, Indore [CSR-IC/CRS-74/2014-15/2104]. Authors thank Dr. M. Gupta and Mr. L. Behra and Dr. A. Banerjee and Mr. K. Kumar, respectively, for XRD and magnetic measurements.

References

- [1] Liu Y, Zhong Y, Zhang J, Ren Z, Cao S, Yang Z, Gao T (2011) Structure and magnetic properties of MnZn nanoferrites synthesized under a high magnetic field. *J Appl Phys* 110:074310–074314
- [2] Eshraghi M, Kameli P (2011) Magnetic properties of CoFe_2O_4 nanoparticles prepared by thermal treatment of ball-milled precursors. *Curr Appl Phys* 11:476–481
- [3] Goldman A (2006) Modern ferrite technology. Springer, Pittsburgh
- [4] Roy PK, Bera J (2006) Effect of Mg substitution on electromagnetic properties of $(\text{Ni}_{0.25}\text{Cu}_{0.20}\text{Zn}_{0.55})\text{Fe}_2\text{O}_4$ ferrite prepared by auto combustion method. *J Magn Magn Mater* 298:38–42
- [5] Mahalakshmi S, SrinivasaManja K, Nithiyanantham S (2014) Electrical properties of nanophase ferrites doped with rare earth ions. *J Supercond Novel Magn* 27:2083–2088
- [6] Reddy MP, Balakrishnaiah G, Madhuri W, Ramana MV, Reddy NR, Siva Kumar KV, Murthy VRK, Reddy RR (2010) Structural, magnetic and electrical properties of NiCuZn ferrites prepared by microwave sintering method suitable for MLCI applications. *J Phys Chem Solids* 71:1373–1380
- [7] Bachhava SG, Patil RS, Ahirrao PB, Patil AM, Patil DR (2011) Microstructure and magnetic studies of Mg–Ni–Zn–Cu ferrites. *Mater Chem Phys* 129:1104–1109
- [8] Sujatha Ch, Reddy KV, Babu KS, Reddy ARC, Suresh MB, Rao KH (2012) Structural and magnetic properties of Mg substituted NiCuZn nano ferrites. *Phys B* 407:1232–1237
- [9] Sujatha Ch, Reddy KV, Babu KS, Reddy ARC, Suresh MB, Rao KH (2013) Effect of Mg substitution on electromagnetic properties of NiCuZn ferrite. *J Magn Magn Mater* 340:38–45
- [10] Sujatha Ch, Reddy KV, Babu KS, Reddy ARC, Suresh MB, Rao KH (2013) Effect of co substitution of Mg and Zn on electromagnetic properties of NiCuZn ferrites. *J Phys Chem Solids* 74:917–923
- [11] Dar MA, Verma V, Gairola SP, Siddiqui WA, Singh RK, Kotnal RK (2012) Low dielectric loss of Mg doped Ni–Cu–Zn nano-ferrites for power applications. *Appl Surf Sci* 258:5342–5347
- [12] Chinnasamy CN, Yang A, Yoon SD, Hsu K, Shultz MD, Carpenter EE, Mukerjee S, Vittoria C, Harris VG (2007) Size dependent magnetic properties and cation inversion in chemically synthesized MnFe_2O_4 nanoparticles. *J Appl Phys* 101:09M509–09M511
- [13] Kapse VD, Ghosh SA, Raghuvanshi FC, Kapse SD (2009) Nanocrystalline spinel $\text{Ni}_{0.6}\text{Zn}_{0.4}\text{Fe}_2\text{O}_4$: a novel material for H_2S sensing. *Mater Chem Phys* 113:638–644
- [14] Weil L, Bertaut EF, Bochirol L (1950) Propriétés magnétiques et structure de la phase quadratique du ferrite de cuivre. *J Phys Radium* 11:208–212
- [15] Tanna AR, Joshi HH (2013) Computer aided X-ray diffraction intensity analysis for spinels: hands-on computing experience. *World Acad Sci Eng Technol* 75:78
- [16] Smit J, Wijn HPJ (1959) Ferrites: Philips Technical Library. Eindhoven, The Netherlands
- [17] Sickafus KE, Wills JM, Grimes NW (1999) Spinel compounds: structure and property relations. *J Am Ceram Soc* 82:3279–3292
- [18] Shannon RD (1976) Revised effective ionic radii and systematic studies of interatomic distances in halides and chalcogenides. *Acta Cryst* A32:751–767
- [19] Qi X, Zhou J, Yue Z, Gui Z, Li L (2003) Permeability and microstructure of manganese modified lithium ferrite prepared by sol–gel auto-combustion method. *Mater Sci Eng B* 99:278–281
- [20] Satalkar M, Kane SN, Ghosh A, Ghodke N, Barrera G, Celegato F, Coisson M, Tiberto P, Vinai F (2014) Synthesis and soft magnetic properties of $\text{Zn}_{0.8-x}\text{Ni}_x\text{Mg}_{0.1}\text{Cu}_{0.1}\text{Fe}_2\text{O}_4$ ($x = 0.0–0.8$) ferrites prepared by sol-gel auto-combustion method. *J Alloys Compd* 615:S313–S316
- [21] Lutterotti L, Scardi P (1990) Simultaneous structure and size-strain refinement by the Rietveld method. *J Appl Cryst* 23:246–252
- [22] Batra AS, Satalkar M, Kane SN, Ghosh A, Ghodke N (2014) Influence of Ni substitution on structural and magnetic properties of $\text{Zn}_{0.85-x}\text{Ni}_x\text{Mg}_{0.05}\text{Cu}_{0.1}\text{Fe}_2\text{O}_4$. *AIP Conf Proc* 1591:537–539
- [23] Costa ACFM, Lula RT, Kiminami RHGA, Gama LFV, de Jesus AA, Andrade HMC (2006) Preparation of nano structured NiFe_2O_4 catalysts by combustion reaction. *J Mater Sci* 41:4871–4875. doi:10.1007/s10853-006-0048-1

- [24] Schneider CA, Rasband WS, Eliceiri KW (2012) NIH Image to ImageJ: 25 years of image analysis. *Nat Methods* 9:671–675
- [25] Chikazumi S (2005) *Physics of ferromagnetism*. Oxford University Press, Oxford
- [26] Stoner EC, Wohlfarth EP (1948) A mechanism of magnetic hysteresis in heterogeneous alloys. *Philos Trans R Soc Lond A* 240:599–642
- [27] Tirosh E, Shemer G, Markovich G (2006) Optimizing cobalt ferrite nanocrystal synthesis using a magneto-optical probe. *Chem Mater* 18:465–470
- [28] Muthuselvam IP, Bhowmik RN (2010) Mechanical alloyed Ho^{3+} doping in CoFe_2O_4 spinel ferrite and understanding of magnetic nanodomains. *J Magn Magn Mater* 322:767–776
- [29] Pearson RF, Annis AD (1968) Anisotropy of Fe^{3+} ions in Yttrium iron garnet. *J Appl Phys* 39:1338–1339
- [30] George M, Nair SS, John AM, Joy PA, Anantharaman MR (2006) Structural, magnetic and electrical properties of the sol-gel prepared $\text{Li}_{0.5}\text{Fe}_{2.5}\text{O}_4$ fine particles. *J Phys D Appl Phys* 39:900–910
- [31] Berkowitz AE, Schuele WJ (1959) Magnetic properties of some ferrite Micropowders. *J Appl Phys* 30:S134–S135
- [32] Verma A, Chatterjee R (2006) Effect of zinc concentration on the structural, electrical and magnetic properties of mixed Mn–Zn and Ni–Zn ferrites synthesized by the citrate precursor technique. *J Magn Magn Mater* 306:313–320
- [33] Panchal S, Raghuvanshi S, Gehlot K, Mazaleyrat F, Kane SN (2016) Cationic distribution assisted tuning of magnetic properties of $\text{Li}_{0.5-x/2}\text{Zn}_x\text{Fe}_{2.5-x/2}\text{O}_4$. *AIP Adv* 6:055930–055936